

Physical Properties of Ba₂Mn₂Sb₂O Single Crystals

J. Li,¹ C. E. Ekuma,^{1,2} I. Vekhter,¹ M. Jarrell,^{1,2} J. Moreno,^{1,2} S. Stadler,¹ A. B. Karki,¹ and R. Jin¹

¹*Department of Physics and Astronomy, Louisiana State University, Baton Rouge, LA 70803, USA*

²*Center for Computation and Technology, Louisiana State University, Baton Rouge, LA 70803, USA*

(Dated: September 14, 2021)

We report both experimental and theoretical investigations of the physical properties of Ba₂Mn₂Sb₂O single crystals. This material exhibits a hexagonal structure with lattice constants: $a = 4.7029(15)$ Å and $c = 19.9401(27)$ Å, as obtained from powder X-ray diffraction measurements, and in agreement with structural optimization through density functional theory (DFT) calculations. The magnetic susceptibility and specific heat show anomalies at $T_N = 60$ K, consistent with antiferromagnetic ordering. However, the magnitude of T_N is significantly smaller than the Curie-Weiss temperature ($|\Theta_{CW}| \approx 560$ K), suggesting a magnetic system of reduced dimensionality. The temperature dependence of both the in-plane and out-of-plane resistivity changes from an activated at $T > T_x \sim 200$ K to a logarithmic at $T < T_x$. Correspondingly, the magnetic susceptibility displays a bump at T_x . DFT calculations at the DFT + U level support the experimental observation of an antiferromagnetic ground state.

PACS numbers: 75.40.Cx, 71.15.Mb, 75.47.Lx, 65.40.Ba

I. INTRODUCTION

The discovery of superconductivity in Fe-based layered compounds has sparked immense interest in the physics and chemistry communities, reminiscent of the excitement that accompanied the discovery of the high- T_c cuprate superconductors more than two decades ago.^{1,2} Although both families form similar layered structures, the building blocks are different, with tetrahedral FeX₄ (X = As, Se) for Fe-based superconductors but octahedral CuO₆ in Cu-based superconductors. In addition, Fe can be partially or even completely replaced by other transition metals,³⁻⁵ while doping on the Cu site of cuprates immediately kills superconductivity.⁶ This suggests that superconductivity in materials with the tetrahedral building block is more tolerant to various dopings.^{3-5,7-10} In particular, magnetic elements such as Co and Ni induce extremely rich phase diagrams including the coexistence of superconductivity and magnetism.⁷⁻¹⁰ In the search for new superconductors with structures similar to the Fe-based materials, but without Fe, BaNi₂As₂ was found to superconduct at 0.7 K.⁴ So far, there is no evidence of superconductivity in Mn-based compounds.

Many Mn-based compounds form layered structures and order magnetically. For example, BaMn₂As₂ shares the same structure with BaFe₂As₂, one of the parent compounds of Fe-based superconductors. Although it orders antiferromagnetically below 625 K,¹¹ its spin structure is different from that of BaFe₂As₂. It is also electrically insulating due to strong spin dependent Mn-As hybridization.¹² Recently, another layered compound, Sr₂Mn₃As₂O₂, has been found to exhibit a spin-glass transition due to competing ferromagnetic and antiferromagnetic interactions.¹³ While it crystallizes in a tetragonal structure, Mn occupies two different environments, one in the MnAs₄ tetrahedra and the other in the MnO₂ sheets.^{14,15} Other compounds with the same structure

such as A₂Mn₃Pn₂O₂ (A = Sr, Ba; Pn = P, As, Sb, Bi) have been synthesized.^{13,16,17} The magnetic moment due to the Mn in edge-shared MnPn₄ orders antiferromagnetically at low temperatures. This motivates us to study Ba₂Mn₂Sb₂O, which has a double layered MnSb₃O tetrahedra edge shared in the *ab*-plane, but corner shared along the *c*-direction (see Fig. 1(a)). All Mn sites are equivalent.

While it has existed since 1981,¹⁴ Ba₂Mn₂Sb₂O is only known to exhibit a hexagonal structure with space group P6₃/mmc. Its physical properties have not yet been investigated. Here, we report the crystal growth, structural, electronic, magnetic, and thermodynamic properties of Ba₂Mn₂Sb₂O. Computational studies have also been carried out to help understand its physical properties.

II. EXPERIMENTAL AND COMPUTATIONAL DETAILS

To grow Ba₂Mn₂Sb₂O single crystals, stoichiometric amounts of high-purity Ba pieces (99 % Alfa Aesar), Mn powder (99.95 % Alfa Aesar), Sb powder (99.5 % Alfa Aesar) and MnO₂ powder (99.997 % Alfa Aesar) are mixed in the ratio 4 : 3 : 4 : 1. The mixture is placed in an alumina crucible sealed in an evacuated quartz tube. The samples are first heated to 1150°C at the rate of 150°C/h. This temperature is held for 15 h, after which the samples are cooled to 700°C at the rate of 4°C/h, and finally cooled down to room temperature by turning off the power. Shiny black plate-like crystals are obtained without requiring additional process. These crystals have a typical size of $5 \times 5 \times 0.2$ mm³, as shown in the inset of Fig. 1(b).

The phase of the as-grown crystals was characterized using a Scintag XDS-2000 powder X-ray diffractometer using Cu K α radiation ($\lambda = 1.54056$ Å). Electrical trans-

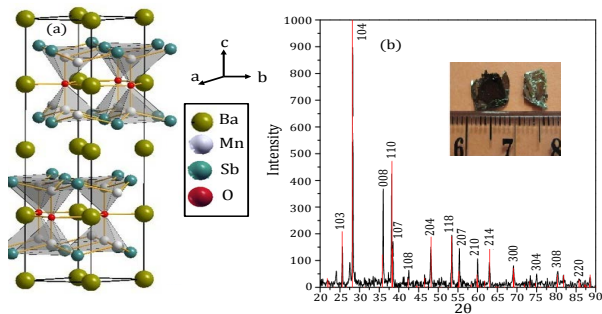


FIG. 1: (Color online) (a) Crystal structure of the layered $\text{Ba}_2\text{Mn}_2\text{Sb}_2\text{O}$; (b) X-ray powder diffraction pattern at room temperature for single crystal $\text{Ba}_2\text{Mn}_2\text{Sb}_2\text{O}$ (black line), which matches well with the standard X-ray powder diffraction pattern (red line). The inset shows single crystal $\text{Ba}_2\text{Mn}_2\text{Sb}_2\text{O}$ with typical size of $5 \text{ mm} \times 5 \text{ mm} \times 0.2 \text{ mm}$.

port and heat capacity measurements were carried out with a Quantum Design physical property measurement system (PPMS). Both in-plane and c-axis resistivities were measured using the standard four-probe technique. Thin Pt wires were used as electrical leads and attached to the sample using silver paste. The magnetic properties were measured using a Quantum Design magnetic property measurement system (MPMS) between 2 and 400 K, and a vibrating sample magnetometer (VSM) between 300 K and 700 K in a PPMS.

We compare the experimental results with the electronic structure calculations. These calculations were performed using the general potential linearized augmented plane wave (LAPW) method¹⁸ as implemented in the WIEN2K electronic structure code.¹⁹ LAPW radii of 2.5 Bohr were used for Ba and Sb, while LAPW radii of 2.01 Bohr and 1.78 Bohr were used for Mn and O, respectively. The calculations were done for the hexagonal crystal structure (space group $P6_3/mmc$) with optimized lattice parameters of $a = 4.7096 \text{ \AA}$ and $c = 20.0298 \text{ \AA}$ obtained from our computations. The unit cell of $\text{Ba}_2\text{Mn}_2\text{Sb}_2\text{O}$ contains two inequivalent Ba sites. Table I shows the locations of these inequivalent Ba sites as well as those of other atoms in the crystal with their Wyckoff positions. The computations were based on $RK_{max} = 7.0$, where R is the smallest LAPW sphere radius and K_{max} is the interstitial plane wave cutoff. The Brillouin zone integration was done using a $9 \times 9 \times 2$ reciprocal space mesh. The core states were treated relativistically, and the spin-orbit interaction was included self-consistently through the second variational step. In all our computations, no shape approximation was made on either the potential or the charge density.

One difficulty in the computation of material properties is that the band gaps and related properties of most materials are generally underestimated by the standard density functional theory (DFT) approximations. To avoid this, we utilized the constrained DFT + U scheme of Anisimov and Gunnarsson²⁰ as implemented by Mad-

sen and Novark²¹ in WIEN2K. With this approach, the effective Coulomb interaction (U_{eff}) on the Mn d state is calculated self-consistently. The computed value of U_{eff} is 7.07 eV. The DFT part of the computation utilized the Perdew-Burke-Ernzerhof generalized gradient approximation (PBE-GGA).²²

III. RESULTS AND DISCUSSION

The X-ray powder diffraction measurements were performed at room temperature by crushing as-grown single crystals. Figure 1(b) shows the X-ray diffraction pattern of $\text{Ba}_2\text{Mn}_2\text{Sb}_2\text{O}$. As indicated in the figure, all peaks can be indexed to the hexagonal structure with space group $P6_3/mmc$ as previously reported.¹⁴ From our X-ray diffraction data, we obtain the lattice parameters: $a = 4.7029 \text{ \AA}$ and $c = 19.9401 \text{ \AA}$ at room temperature, in agreement with that reported by Brechtel et al.¹⁴

Figure 2(a) displays the temperature dependence of in-plane (ρ_{ab}) and out-of-plane (ρ_c) resistivities of $\text{Ba}_2\text{Mn}_2\text{Sb}_2\text{O}$ between 2 and 320 K. Note both ρ_{ab} and ρ_c increase with decreasing temperature. However, the change is much slower below $T_x \sim 200 \text{ K}$ than it is at high temperatures. Correspondingly, the anisotropy, ρ_c/ρ_{ab} , is almost constant below T_x as shown in the inset of Fig. 2(a), and is comparable to that seen in the AFe_2As_2 ($A = \text{Ba, Sr, Ca}$) system.²³ As shown in Fig. 2(b), the application of a magnetic field, $H = 7 \text{ T}$, normal to the ab plane ($H \perp ab$) results in a small reduction of ρ_{ab} . This means that the magnetoresistance, $MR = \frac{\rho_{ab}(H) - \rho_{ab}(0)}{\rho_{ab}(0)}$, is negative, as shown in the inset of Fig. 2(b). Note the magnitude of MR decreases more rapidly below $\sim 60 \text{ K}$.

In analyzing the temperature dependence of the electrical resistivity, we find that both $\rho_{ab}(T)$ and $\rho_c(T)$ exhibit quantitatively similar behaviors. Figure 2(c) shows ρ_{ab} versus $\ln T$, which reveals a logarithmic dependence below T_x . From 2 to 200 K we obtain $\rho_{ab} = -2.64 \ln T + 104.6 \text{ \Omega-cm}$, plotted as a solid line in Fig. 2(c). Above T_x the resistivity decreases exponentially, so that we fit the in-plane electrical conductivity data as shown in Fig. 2(d) using the formula for the conductivity, $\sigma_{ab} = \sigma_0 + B \exp(-\frac{\Delta}{2k_B T})$ (σ_0 and B are constants, k_B is the Boltzmann constant, and Δ is the activation energy). The fit (see the solid line in Fig. 2(d)) yields $\sigma_0 = 0.086 \text{ \Omega}^{-1}\text{cm}^{-1}$, $B = 2095 \text{ \Omega}^{-1}\text{cm}^{-1}$, and $\Delta \sim 0.59 \text{ eV}$. A similar gap value of $\Delta_c \sim 0.61 \text{ eV}$ was obtained from fitting ρ_c (not shown).

The crossover from the activated to the much slower increase in resistivity at low temperatures indicates that the system has a finite (albeit low) carrier density as T approaches zero. However, the low-temperature logarithmic behavior of both ρ_{ab} and ρ_c suggests an anomalous temperature dependence of the scattering rate for the remaining carriers. The magnetic properties shown below (see Fig. 3) may offer a clue to the origin of this scatter-

TABLE I: The atomic positions and the Wyckoff numbers for the atoms in Ba₂Mn₂Sb₂O. Experimental data is adapted from Ref. 14.

Site	Wyckoff	Symmetry	Charge	x	y	z	Atomic environment
Experimental atomic positions							
Mn1	4f	3m.	Mn2+	$\frac{1}{3}$	$\frac{2}{3}$	0.6495	single atom O
Sb2	4f	3m.	Sb3-	$\frac{1}{3}$	$\frac{2}{3}$	0.3873	non-coplanar triangle Mn ₃
O1	2d	-6m2	O2-	$\frac{1}{3}$	$\frac{2}{3}$	$\frac{3}{4}$	trigonal bipyramid Mn ₂ Ba ₃
Ba4	2b	-6m2	Ba2+	0	0	$\frac{1}{4}$	coplanar triangle O ₃
Ba5	2a	-3m	Ba2+	0	0	0	octahedron Sb ₆
Atomic positions as obtained from geometrical optimization							
Mn1	4f	3m.	Mn2+	$\frac{1}{3}$	$\frac{2}{3}$	0.6506	single atom O
Sb2	4f	3m.	Sb3-	$\frac{1}{3}$	$\frac{2}{3}$	0.39467	non-coplanar triangle Mn ₃
O1	2d	-6m2	O2-	$\frac{1}{3}$	$\frac{2}{3}$	$\frac{3}{4}$	trigonal bipyramid Mn ₂ Ba ₃
Ba4	2b	-6m2	Ba2+	0	0	$\frac{1}{4}$	coplanar triangle O ₃
Ba5	2a	-3m	Ba2+	0	0	0	octahedron Sb ₆

ing.

The magnetic susceptibility $\chi = M/H$ was measured at an applied magnetic field $H = 1$ kOe between 2 and 700 K. Figure 3 shows the temperature dependence of the in-plane (χ_{ab}) and the out-of-plane (χ_c) susceptibilities in zero-field-cooling (zfc) and field-cooling (fc) conditions. Several features are worth noticing: (1) there is almost no difference between $\chi(H||ab)$ and $\chi(H||c)$ above ~ 60 K, i.e., the susceptibility is isotropic; (2) below 60 K $\chi(H||ab)$ decreases while $\chi(H||c)$ increases; and (3) there is a broad bump in χ_{ab} and χ_c centered around $T \sim T_x$. These features are reminiscent of another transition-metal oxide K₂V₃O₈.²⁴ While it is a two-dimensional antiferromagnet, its magnetic susceptibility remains isotropic above T_N . According to Lumsden et al.²⁴, this is the consequence of Heisenberg magnetic interactions. The bump seen in the magnetic susceptibility of K₂V₃O₈ is due to competition between the antisymmetric Dzyaloshinskii-Moriya (DM) interaction and the symmetric Heisenberg interaction. The competition may also result in a canted magnetic structure. For Ba₂Mn₂Sb₂O, it is unclear whether the DM interaction should be taken into account. However the increase of χ_c below T_N suggests that spins are canted as well in Ba₂Mn₂Sb₂O, which gives rise to weak ferromagnetism along the c-direction. This is further supported by the non-linear field dependence of c-axis magnetization below T_N (not shown). On the other hand, the characteristic temperature where χ shows a bump coincides with the crossover temperature, T_x , where the resistivities (ρ_{ab} and ρ_c) change their temperature dependence. As will be discussed later, this suggests that there may be another mechanism to cause the change in both the magnetic susceptibility and electrical resistivity.

Fitting the data above 350 K with a Curie-Weiss expression $\chi = \chi_o + \frac{C_{CW}}{T - \Theta_{CW}}$ (χ_o , C_{CW} , and Θ_{CW} are constants), we obtain $\Theta_{CW} = -564$ K, $C_{CW} = 9.24$ cm³ K/mol, and $\chi_o = -6.6 \times 10^{-5}$ cm³/mol (see the solid line

in Fig. 3). With a Curie-Weiss constant $C_{CW} = \frac{N_A \mu_{eff}^2}{3k_B}$, we estimate the effective magnetic moment, $\mu_{eff} = 2.7 \mu_B/\text{f.u.}$ The negative Θ_{CW} suggests antiferromagnetic correlations at high temperatures leading to long-range antiferromagnetic ordering at $T_N \sim 60$ K. As shown in the inset of Fig. 3, χ_{ab} decreases, indicating that ordered magnetic moments are in the $a - b$ -plane. The fact that Θ_{CW} is much higher than T_N suggests low-dimensional magnetism, because the given crystal structure is not likely to cause magnetic frustration.

To confirm the phase transition at T_N , we have measured the specific heat of Ba₂Mn₂Sb₂O at constant pressure. As shown in Fig. 4, there is clearly an anomaly at T_N , an indication of a phase transition. If we estimate the background by fitting the data away from T_N , as shown in the inset of Fig. 4 by the dashed line, we can obtain the specific heat change ΔC_p due to the phase transition. By integrating $\int \frac{\Delta C_p}{T} dT$, we find an entropy change $\Delta S \sim 1.55$ J/mol-K. This value is much smaller than the theoretical expectation $S_M = R \ln(2S + 1) = 14.9$ J/mol-K, ($R = 8.314$ J/mol-K, with full moment $S = 5/2$ for Mn²⁺). This implies that the entropy is either removed prior to the transition and/or results from a reduced effective magnetic moment.

To help understand these experimental results we have performed first-principles ab-initio electronic structure computations. In order to establish the ground state of Ba₂Mn₂Sb₂O, we carried out calculations on several configurations: ferromagnetic, antiferromagnetic, and non-magnetic. The results of our computations show that the antiferromagnetic state is the most stable one. We used the A-type antiferromagnetic alignment, i.e., the magnetic structure having ferromagnetic alignment in-planes but antiferromagnetic coupling between planes. In this structure, no supercell is needed.^{25,26} Fig. 5(a) depicts the band structure of Ba₂Mn₂Sb₂O along the high symmetry points of the Brillouin zone, while Figure 5(b)

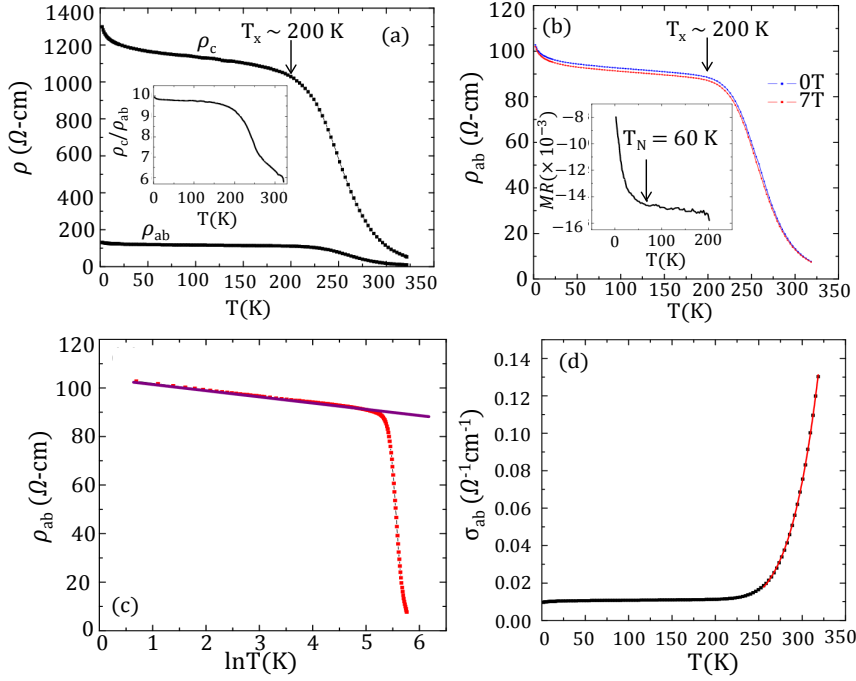


FIG. 2: (Color online) (a) In-plane (ρ_{ab}) and out-of-plane (ρ_c) resistivities of Ba₂Mn₂Sb₂O single crystal. The inset shows the temperature dependence of resistivity anisotropy (ρ_c/ρ_{ab}); (b) Temperature dependence of ρ_{ab} under zero and 7 T applied perpendicular to the ab -plane. The inset shows the temperature MR dependence of magnetoresistivity MR (see the text); (c) In-plane resistivity plotted as ρ_{ab} versus $\ln T$. The solid line is the fit of ρ_{ab} below 200 K (see the text); (d) Temperature dependence of the in-plane conductivity (σ_{ab}). The red line is the fit of σ_{ab} above 250 K with $\sigma_{ab} = \sigma_0 + B \exp(-\frac{\Delta}{2k_B T})$.

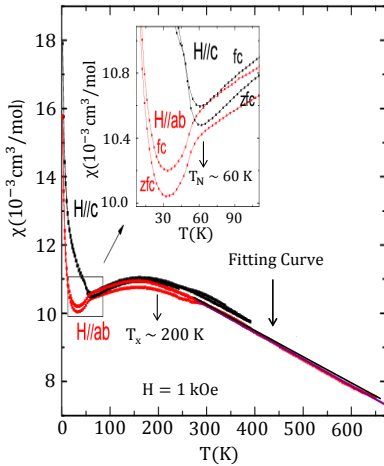


FIG. 3: (Color online) Temperature dependence of magnetic susceptibility on the ab -plane (χ_{ab}) and along the c -direction (χ_c) measured under both zero-field-cooling (zfc) and field-cooling (fc) conditions. The characteristic temperature T_x is indicated. The inset shows $\chi_{ab}(T)$ and $\chi_c(T)$ near $T_N \sim 60$ K.

shows the density of states.

The conduction bands are predominantly Mn 3d states while the valence bands are formed by a strong hybridization between Mn 3d and Sb 5p with O 2p at ~ 2.5 eV below the bottom of the conduction band. Also, we find a very large energy difference, $E_{Diff} = 0.21$ eV/Mn, between the ferromagnetic (the next stable state) and antiferromagnetic (ground state phase) orderings. This indeed is supported by the large Curie-Weiss temperature

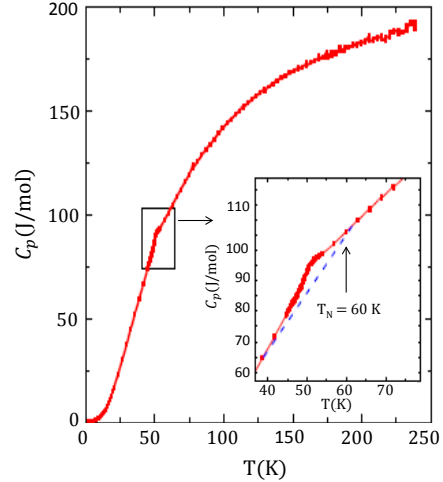


FIG. 4: (Color online) Temperature dependence of the specific heat, C_p . The inset shows the anomaly near T_N , and the dash line represents the background.

($|\Theta_{CW}| \approx 560$ K) extracted from the high-temperature susceptibility. The maximum of the valence bands occurs at the Γ point and the minimum of the conduction bands is at the M point. The minimal indirect gap between M and Γ is 0.686 eV, in close agreement with the experimental values of 0.59 and 0.61 eV deduced from the conductivity σ_{ab} and σ_c , respectively. The effective mass in the conduction band is $m^* \sim 4.09 m_o$ (where m_o is the bare electron mass). In the valence band, the effective mass tensor is rather anisotropic but the masses are of the same order. We also calculated the magnetic moment per formula unit. The computed effective mag-

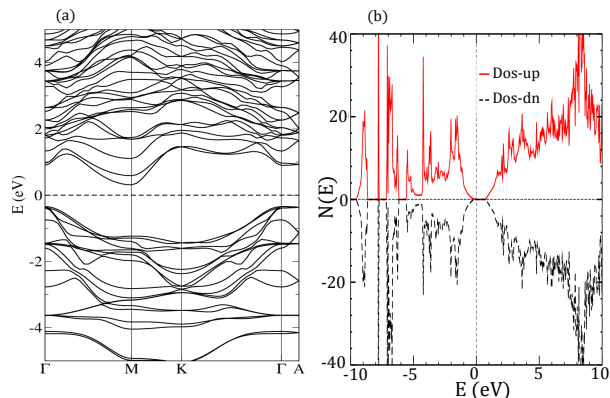


FIG. 5: (Color online). (a) Calculated band structure of $\text{Ba}_2\text{Mn}_2\text{Sb}_2\text{O}$. The horizontal dotted line is the chemical potential, which has been set equal to zero. (b) Calculated density of states (in units of states/eV-cell) of $\text{Ba}_2\text{Mn}_2\text{Sb}_2\text{O}$. Both figures have been produced by using the effective Coulomb interaction (U_{eff}) obtained self-consistently at the DFT+U level.

netic moment $\mu_{eff} = 2.52 \mu_B/\text{f.u.}$, is in good agreement with the experimental value of $2.7 \mu_B/\text{f.u.}$ obtained from a Curie-Weiss fit to the high temperature susceptibility. Treating the compound as an intrinsic semiconductor, we obtain a rough estimate of the carrier concentration at room temperature $n_T \sim 3.5 \times 10^{14} \text{ cm}^{-3}$ using the computed gap, or an order or magnitude greater if we take the gap values from the resistivity fit above. Simple estimate of the Drude relaxation time using the former value of the carrier density yields $\tau \sim 4.5 \times 10^{-12} \text{ s}$. The carrier mobility at room temperature is $\mu = \sigma/ne \sim 2 \times 10^3 \text{ cm}^2\text{V}^{-1}\text{s}^{-1}$. Residual conductivity at low T indicates that there are mobile carriers that are not induced by temperature, but their density is low: even if we take the value of the room temperature mobility as a guide, the non-intrinsic carrier density $n_i \sim 10^{13} \text{ cm}^{-3}$ is sufficient to give the residual ρ_{ab} . In reality, the mobility likely grows by more than an order of magnitude as the temperature is lowered, and therefore an even lower carrier density suffices. Self-consistent structural and geometrical optimization yields lattice parameters: $a = 4.7096 \text{ \AA}$ and $c = 20.0298 \text{ \AA}$. These are consistent with the values determined experimentally. The geometrical optimization reproduced the atomic positions of $\text{Ba}_2\text{Mn}_2\text{Sb}_2\text{O}$ as shown in Table I.

From the above comparison, we note that the computed results are consistent with those obtained experimentally. In particular, the computed effective moment is very close to the experimental value obtained from the Curie-Weiss fit. While Mn^{2+} can be in high-spin ($S = 5/2$), intermediate ($S = 3/2$), or low-spin ($S = 1/2$) states, it is possible that there is a partial cancellation of the spin by an antialigned moment from

the Sb 5p band of the Sb_3O cage surrounding Mn, as seen in $\text{Yb}_{14}\text{MnSb}_{11}$.²⁷ According to the X-ray magnetic circular dichroism (XMCD) measurements, the Sb_4 cage in $\text{Yb}_{14}\text{MnSb}_{11}$ provides a moment $S = 1$ opposite to the Mn moment²⁷ due to hybridization between the Mn 3d and Sb 5p orbitals.²⁸ The strong hybridization of Sb 5p with Mn 3d is confirmed by our computations as explained above. In our ab-initio calculations, the magnetic moment of Sb is found to be significant with an antialigned moment of $\sim -0.1 \mu_B$ as observed in $\text{Yb}_{14}\text{MnSb}_{11}$.²⁷ If we assume that the induced magnetic moment of the Sb_3O cage is slightly less than $S = 1$, and Mn^{2+} is in the intermediate spin state ($S = 3/2$), the effective magnetic moment would be close to our experimental and calculated results. For each MnPn_4 ($\text{Pn} = \text{P, As, Sb, and Bi}$), accompanying the induced magnetic moment, there is a hole per formula unit in the bonding valence bands.²⁹ We anticipate a similar situation in $\text{Ba}_2\text{Mn}_2\text{Sb}_2\text{O}$. The effective hole concentration for each MnSb_3O could be slightly different from that of MnPn_4 . The question is whether these holes interact with the local magnetic moment provided by Mn^{2+} (i.e., Kondo effect), as seen in $\text{Yb}_{14}\text{MnSb}_{11}$.^{30,31} The logarithmic temperature dependence of the electrical resistivity (see Fig. 2(c)), and the decrease of magnetic susceptibility (see Fig. 3) below $\sim 200 \text{ K}$, seem to be consistent with the Kondo picture.

IV. CONCLUSION

We have studied the structural, electronic, magnetic, and thermodynamic properties of $\text{Ba}_2\text{Mn}_2\text{Sb}_2\text{O}$ single crystals. This compound exhibits semiconductor behavior with thermally activated electrical conduction at high temperatures, where the energy gap was found to be $\sim 0.59 \text{ eV}$ from experiment and $\sim 0.686 \text{ eV}$ from band calculations. The magnetic susceptibility reveals a bump at $T_x \sim 200 \text{ K}$ and an antiferromagnetic transition at $T_N \sim 60 \text{ K}$. The latter was confirmed by specific heat measurements, indicating a true phase transition. While the present analysis and discussion is in no way conclusive, we hope that it will spur interest to further study this material.

Acknowledgments

Research is in part supported by the National Science Foundation (NSF) Award Numbers DMR-1002622 (J.L., A.K., and R.J.), NSF LA-SIGMA EPS-1003897 (C.E.E., M.J., I.V., and J.M.), and NSF DMR-0965009 (S.S.) High performance computational resources are provided by the Louisiana Optical Network Initiative (LONI).

-
- ¹ Y. Kamihara, H. Hiramatsu, M. Hirano, R. Kawamura, H. Yanagi, T. Kamiya, and T. Hosono, *J. Am. Chem. Soc.* **128**, 10012 (2006).
- ² J. G. Bednorz and K. A. Müller, *Phys. B: Cond. Matter* **64**, 189 (1986).
- ³ A. S. Sefat, R. Jin, M. A. McGuire, B. C. Sales, D. J. Singh, and D. Mandrus, *Phys. Rev. Lett.* **101**, 117004 (2008).
- ⁴ A. S. Sefat, M. A. McGuire, R. Jin, B. C. Sales, D. Mandrus, F. Ronning, E. D. Bauer, and Y. Mozharivskyj, *Phys. Rev. B* **79**, 094508 (2009).
- ⁵ Anupam, V. K. Anand, P. L. Paulose, S. Ramakrishnan, C. Geibel, and Z. Hossain, *Phys. Rev. B* **85**, 144513 (2012).
- ⁶ C. U. Jung, J. Y. Kim, M.-S. Park, M.-S. Kim, H.-J. Kim, S. Y. Lee, and S.-I. Lee, *Phys. Rev. B* **65**, 172501 (2002).
- ⁷ S. Nandi, M. G. Kim, A. Kreyssig, R. M. Fernandes, D. K. Pratt, A. Thaler, N. Ni, S. L. Bud'ko, P. C. Canfield, J. Schmalian, et al., *Phys. Rev. Lett.* **104**, 057006 (2010).
- ⁸ N. Ni, A. Thaler, J. Q. Yan, A. Kracher, E. Colombier, S. L. Bud'ko, P. C. Canfield, and S. T. Hannahs, *Phys. Rev. B* **82**, 024519 (2010).
- ⁹ Z. Guguchia, J. Roos, A. Shengelaya, S. Katrych, Z. Bukowski, S. Weyeneth, F. Murányi, S. Strässle, A. Maisuradze, J. Karpinski, et al., *Phys. Rev. B* **83**, 144516 (2011).
- ¹⁰ M. Matusiak, Z. Bukowski, and J. Karpinski, *Phys. Rev. B* **83**, 224505 (2011).
- ¹¹ Y. Singh, M. A. Green, Q. Huang, A. Kreyssig, R. J. McQueeney, D. C. Johnston, and A. I. Goldman, *Phys. Rev. B* **80**, 100403 (2009).
- ¹² J. An, A. S. Sefat, D. J. Singh, and M.-H. Du, *Phys. Rev. B* **79**, 075120 (2009).
- ¹³ R. Nath, V. O. Garlea, A. I. Goldman, and D. C. Johnston, *Phys. Rev. B* **81**, 224513 (2010).
- ¹⁴ E. Brechtel, G. Cordier, and H. Schäfer, *Z. Naturforsch. B* **36**, 27 (1981).
- ¹⁵ T. C. Ozawa and S. M. Kauzlarich, *Sci. Technol. Adv. Mater.* **9**, 033003 (2008).
- ¹⁶ N. T. Stetson and S. M. Kauzlarich, *Inorg. Chem.* **30**, 3969 (1991).
- ¹⁷ E. Brechtel, G. Cordier, and H. Schäfer, *Z. Naturforsch. B* **34**, 777 (1979).
- ¹⁸ D. J. Singh, *Planewaves, Pseudopotentials, and the LAPW Method, 2nd Ed.* (Springer-Verlag, Berlin, 2006).
- ¹⁹ P. Blaha, K. Schwarz, G. Madsen, D. Kvasnicka, and J. Luitz, *WIEN2K, An Augmented Plane Wave+Local Orbitals Program for Calculating Crystal Structure* (K. Schwarz Technical University, Wien, Austria, 2001).
- ²⁰ V. I. Anisimov and O. Gunnarsson, *Phys. Rev. B* **43**, 7570 (1991).
- ²¹ G. K. H. Madsen and P. Novark, *Europys. Lett.* **69**, 777 (2005).
- ²² J. P. Perdew, K. Burke, and M. Ernzerhof, *Phys. Rev. Lett.* **77**, 3865 (1996).
- ²³ M. A. Tanatar, N. Ni, G. D. Samolyuk, S. L. Bud'ko, P. C. Canfield, and R. Prozorov, *Phys. Rev. B* **79**, 134528 (2009).
- ²⁴ M. D. Lumsden, B. C. Sales, D. Mandrus, S. E. Nagler, and J. R. Thompson, *Phys. Rev. Lett.* **86**, 159 (2001).
- ²⁵ Y. Sekine, H. Takahashi, N. Mori, T. Matsumoto, and T. Kosaka, *Physica B: Condensed Matter* **48**, 237 (1997).
- ²⁶ C. E. Ekuma, et al. Manuscript in preparation.
- ²⁷ A. P. Holm, S. M. Kauzlarich, S. A. Morton, G. D. Waddiu, W. E. Pickett, and J. G. Tobin, *J. Am. Chem. Soc.* **124**, 9894 (2002).
- ²⁸ A. Kimura, S. Suga, T. Shishidou, S. Imada, T. Muro, S. Y. Park, T. Miyahara, T. Kaneko, and T. Kanomata, *Phys. Rev. B* **56**, 6021 (1997).
- ²⁹ D. Sánchez-Portal, R. M. Martin, S. M. Kauzlarich, and W. E. Pickett, *Phys. Rev. B* **65**, 144414 (2002).
- ³⁰ K. S. Burch, A. Schafgans, N. P. Butch, T. A. Sayles, M. B. Maple, B. C. Sales, D. Mandrus, and D. N. Basov, *Phys. Rev. Lett.* **95**, 046401 (2005).
- ³¹ B. C. Sales, P. Khalifah, T. P. Enck, E. J. Nagler, R. E. Sykora, R. Jin, and D. Mandrus, *Phys. Rev. B* **72**, 205207 (2005).